

2

AD-A235 938



Time-Resolved Mass and Energy Analysis

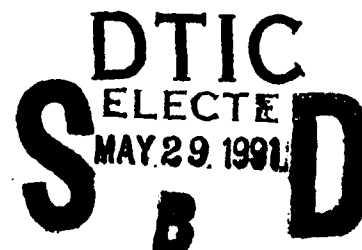
Prepared by

J. E. POLLARD, D. A. LICHTIN, S. W. JANSON, and R. B. COHEN
Aerophysics Laboratory
Laboratory Operations

8 April 1991

Prepared for

SPACE SYSTEMS DIVISION
AIR FORCE SYSTEMS COMMAND
Los Angeles Air Force Base
P. O. Box 92960
Los Angeles, CA 90009-2960



Engineering and Technology Group

THE AEROSPACE CORPORATION
El Segundo, California

APPROVED FOR PUBLIC RELEASE;
DISTRIBUTION UNLIMITED

DEFENSE TECHNICAL INFORMATION CENTER



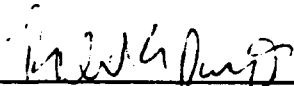
9100522

91 0 24 043

This report was submitted by The Aerospace Corporation, El Segundo, CA 90245-4691, under Contract No. F04701-88-C-0089 with the Space Systems Division, P. O. Box 92960, Los Angeles, CA 90009-2960. It was reviewed and approved for The Aerospace Corporation by W. P. Thompson, Jr., Director, Aerophysics Laboratory. Lt Day was the project officer for the Mission-Oriented Investigation and Experimentation (MOIE) program.

This report has been reviewed by the Public Affairs Office (PAS) and is releasable to the National Technical Information Service (NTIS). At NTIS, it will be available to the general public, including foreign nationals.

This technical report has been reviewed and is approved for publication. Publication of this report does not constitute Air Force approval of the report's findings or conclusions. It is published only for the exchange and stimulation of ideas.



ROBERT DAY, Lt, USAF
MOIE Project Officer
SSD/CLUD



JONATHAN M. EMMES, Maj, USAF
MOIE Manager Program
PL/WCO OL-AB

UNCLASSIFIED

SECURITY CLASSIFICATION OF THIS PAGE

REPORT DOCUMENTATION PAGE				
1a. REPORT SECURITY CLASSIFICATION Unclassified		1b. RESTRICTIVE MARKINGS		
2a. SECURITY CLASSIFICATION AUTHORITY		3. DISTRIBUTION/AVAILABILITY OF REPORT		
2b. DECLASSIFICATION/DOWNGRADING SCHEDULE		Approved for public release; distribution unlimited.		
4. PERFORMING ORGANIZATION REPORT NUMBER(S) TR-0089(4930-02)-1		5. MONITORING ORGANIZATION REPORT NUMBER(S) SD-TR-91-11		
6a. NAME OF PERFORMING ORGANIZATION The Aerospace Corporation Laboratory Operations	6b. OFFICE SYMBOL (if applicable)	7a. NAME OF MONITORING ORGANIZATION Space Systems Division Air Force Systems Command		
6c. ADDRESS (City, State, and ZIP Code) 2350 E. El Segundo Blvd. El Segundo, CA 90245		7b. ADDRESS (City, State, and ZIP Code) Los Angeles Air Force Base P.O. Box 92960 Los Angeles, CA 90019-2960		
8a. NAME OF FUNDING/SPONSORING ORGANIZATION	8b. OFFICE SYMBOL (if applicable)	9. PROCUREMENT INSTRUMENT IDENTIFICATION NUMBER F04701-88-C-0089		
8c. ADDRESS (City, State, and ZIP Code)		10. SOURCE OF FUNDING NUMBERS		
		PROGRAM ELEMENT NO.	PROJECT NO.	TASK NO.
				WORK UNIT ACCESSION NO.
11. TITLE (Include Security Classification) Time-Resolved Mass and Energy Analysis				
12. PERSONAL AUTHOR(S) J. E. Pollard, D. A. Lichtin, S. W. Janson, and R. B. Cohen				
13a. TYPE OF REPORT	13b. TIME COVERED FROM _____ TO _____	14. DATE OF REPORT (Year, Month, Day) 8 April 1991	15. PAGE COUNT 39	
16. SUPPLEMENTARY NOTATION-				
17. COSATI CODES			18. SUBJECT TERMS (Continue on reverse if necessary and identify by block number)	
FIELD	GROUP	SUB-GROUP		
			Energy Analysis Position-Sensitive Detection	
			Mass Spectrometry Time-of-Flight Mass Spectrometry	
19. ABSTRACT (Continue on reverse if necessary and identify by block number)				
A new method for time-resolved mass and kinetic energy analysis of ionic or neutral species in the range of 1 to 150 amu and 0.5 to 500 eV is described. Time-of-flight mass spectrometry is combined with position-sensitive detection to measure energy spectra for multiple masses at burst-mode sampling rates as high as 50 kHz. The detector is a rectangular microchannel plate with a 96-element metal anode array that is read out either by fast analog-to-digital converters or by discriminators and scalars. The apparatus is configured so that the measured ion drift time varies as the square root of the mass-to-charge ratio and the displacement along the detector varies as the square root of the energy-to-charge ratio. Applications are envisioned in plasma analysis, in beam-scattering experiments, and in diagnostic measurements for spacecraft propulsion.				
20. DISTRIBUTION/AVAILABILITY OF ABSTRACT		21. ABSTRACT SECURITY CLASSIFICATION		
<input checked="" type="checkbox"/> UNCLASSIFIED/UNLIMITED <input type="checkbox"/> SAME AS RPT. <input type="checkbox"/> DTIC USERS		Unclassified		
22a. NAME OF RESPONSIBLE INDIVIDUAL		22b. TELEPHONE (Include Area Code)	22c. OFFICE SYMBOL	

PREFACE

We acknowledge the important contributions made by R. Rianda during the conceptual phase of this work. The apparatus was constructed with the assistance of D. R. Schulthess, J. R. Hiatt, and C. T. Colborne.



Accession For	
NTIS GRA&I	<input checked="" type="checkbox"/>
DTIC TAB	<input type="checkbox"/>
Unannounced	<input type="checkbox"/>
Justification	
By _____	
Distribution/ _____	
Availability Codes	
Dist	Avail and/or Special
A-1	

CONTENTS

PREFACE.....	1
I. INTRODUCTION.....	7
II. CONCEPT.....	11
III. CONSTRUCTION.....	17
A. Vacuum System.....	17
B. Multianode MCP Detector.....	17
C. Preamplifiers.....	20
D. Fast-Analog Electronics.....	21
E. Ion-Counting Electronics.....	23
IV. PERFORMANCE.....	25
A. Gain vs. Position.....	25
B. Cross-Talk.....	25
C. Ion Beams.....	27
D. Neutral Beams.....	29
E. Resolution.....	33
REFERENCES.....	39

FIGURES

1. Analyzer Concept and Distance Parameters for Time-of-Flight Mass Spectrometry.....	12
2. Time-of-Flight Analyzer with Detector Chamber and Differentially Pumped Source.....	18
3. Circuits for the Microchannel Plate Biasing, Signal Decoupling, and Preamplification.....	19
4. Data Collection Electronics for the Time-of-Flight Analyzer in the Fast-Analog Mode of Detection.....	22
5. Spatial Dependence of the Detector Response as Measured with a Scanned, Collimated Ion Beam and with a Diffuse, Pseudouniform Ion Beam.....	26
6. Position-Sensitive Detector Output for Ar ⁺ Beams with Nominal Kinetic Energies Between 10 and 45 eV Recorded by Ion Counting Detection.....	28
7. Energy Calibration Data for Ar ⁺ Beams with Four Different TOFMS Drift Energies.....	30
8. Position-Integrated IOFMS Waveform for a Pulsed Neutral Beam Containing Ne and Kr Seeded in H ₂ , as Measured Near the Peak of a 450- μ s-Duration Gas Pulse.....	32
9. Sequential TOFMS Waveform Taken with a 40 kHz Burst Rate During a Gas Pulse Containing Ne and Kr Seeded in H ₂	34
10. Time-Resolved Energy Spectra for ⁸⁴ Kr Recorded at 25 μ s Intervals.....	35
11. Calculated Ion Trajectories Showing Deflection by Field Distortions Near the Grid Wires Covering the Slit in the Mass Energy Analyzer.....	36

1. INTRODUCTION

Techniques for simultaneously measuring the masses and kinetic energies of ions and neutral molecules have applications in many areas of physics and chemistry, including diagnostic experiments for fusion plasmas,¹ beam-foil and crossed-beam scattering,^{2,3} ablation of surfaces by particle beams or lasers,⁴ and the analysis of space plasmas in the near-earth environment and beyond.^{5,6} Our interest in this area derives from the need for definitive ground-based measurements of plume flow-fields from spacecraft electric propulsion devices such as electrothermal arcjets,⁷ electromagnetic plasma thrusters,⁸ and electrostatic ion engines.⁹

A plume diagnostic experiment is performed in a large high-vacuum chamber by analyzing the masses and energies of plume species over a range of angles encompassing the forward-flow and the backward-flow regions. Such information can lead to improvements in performance and reliability and can also measure the potential for contamination of critical spacecraft surfaces by the thruster. Ideally the mass energy analyzer would be capable of moving about within the unperturbed plume, but generally a more practical solution is to skim off a portion of the flow into a differentially pumped detector chamber and to obtain the angular data by rotating the thruster. Fast time-resolved sampling can be beneficial in detecting transient phenomena and for discriminating against chamber wall effects with thrusters that operate in a pulsed mode. Here a measurement of the plume species arrival time can be used to reject signals caused by fast wall-scattered molecules, since their arrival times will be incommensurate with the mass and energy measured by the analyzer. Thus, it becomes possible to study the low-velocity backward-flow component of the plume that is of particular importance from the standpoint of spacecraft contamination.

A pulsed-plasma thruster using solid Teflon as the propellant poses a very challenging set of requirements for a plume diagnostic experiment.¹⁰ In this device the surface of a Teflon bar is ablated by a discharge from a capacitor bank, and the resulting plasma is electromagnetically accelerated by the discharge current. The plume may contain a variety of neutral and ionic fragments derived from the $(CF_2)_n$ polymer with kinetic energies from 0.5 to 500 eV. Although the duration of the discharge is only 20 μ s, several

milliseconds may elapse between the start of the discharge and the arrival of the slowest plume species at detector. The low repetition rate of this thruster (typically 0.2 Hz) makes it desirable to record a complete time-resolved mass and energy data set on each thruster firing, so that the shot-to-shot reproducibility can be measured.

Electric and magnetic dispersing fields have been combined in a variety of ways to achieve simultaneous mass and energy analysis.¹¹⁻¹⁴ The time-resolution of these analyzers is enhanced by placing multiple detection channels in parallel along the energy axis, although a separate set of channels is required for each mass that is to be detected simultaneously. The Thomson parabola spectrometer¹⁵⁻¹⁷ is perhaps the simplest type to construct, but the parabolic nature of the mass and energy dispersion makes it cumbersome to use when multichannel detection is required. A more convenient arrangement is provided by so-called E-parallel-B spectrometers,¹⁸⁻²³ which (when combined with a charge exchange cell) have seen frequent use at magnetic confinement fusion laboratories for analysis of H and D neutrals in the 1 to 100 keV energy range. E-parallel-B spectrometers are readily adapted to multichannel ion-counting detection and have the ability to probe events on a time scale as short as 1 ms. One other approach uses electrostatic deflection and quadrupole mass spectrometry to measure the time-resolved neutral or ion flux for a specific energy and mass.⁴ Time-of-flight techniques have also been applied to mass and energy measurements with plasmas and particle beams.^{5,24-26} A significant feature of time-of-flight is that the number of detection channels does not need to be as large as with comparable electric/magnetic dispersing instruments, because one of the parameters being measured (either mass or energy) is dispersed temporally rather than spatially. There is a significant advantage to temporal dispersion of mass in propulsion diagnostic applications where a wide range of chemical species must be detected simultaneously.

A new method for time-resolved mass and energy analysis of ions or neutrals in the range of 1 to 150 amu and 0.5 to 500 eV is reported here. This approach uses time-of-flight mass spectrometry with position-sensitive detection in an arrangement where the ion drift time varies as the square root of the mass-to-charge ratio and the displacement along the detector varies as the square root of the energy-to-charge ratio. A burst-mode sampling rate as high as 50 kHz (20 μ s time resolution) is achieved by a unique fast-analog

detection scheme with a multianode microchannel plate. When ion counting detection is more appropriate, the readout is performed with a set of discriminators and scalers. The analyzer concept is described in Section II, an overview of the construction of the instrument is given in Section III, and the calibration data obtained with test sources of ionic and neutral beams are reported in Section IV.

II. CONCEPT

Time-of-flight mass spectrometers (TOFMS) with first-order space-focusing^{27,28} have found uses in many applications where speed of response and ease of construction are of critical importance. The new feature of the present TOFMS analyzer is the application of position-sensitive detection to the simultaneous measurement of masses and energies. As shown in Figure 1, ions with mass-to-charge ratio m/q and energy $U_x = (1/2)mv_x^2$ enter the analyzer between two grounded plates. A voltage pulse is applied to the repeller plate to create an electric field E_s that accelerates the ions through the opening in the slit plate. The ions are accelerated by a second field E_d before entering the field-free drift region that terminates at the position-sensitive detector. The velocity v_y imparted by the electric fields is perpendicular to the incident velocity v_x . Thus, all the ions of a given m/q arrive at the detector at the same time (independent of v_x) with a displacement along the detector that is proportional to v_x . The repeller pulse amplitude and the drift tube voltage are adjusted for first order space-focusing, meaning that the arrival time of a given m/q ion at the detector is nearly independent of s , the initial distance between the ion and the slit plate.

Low energy ions in the extraction region could be perturbed if there were significant penetration of the field E_d through the slit. To minimize this effect, grids are attached to both surfaces of the slit plate as indicated in Figure 1. The equations for analyzing space-focusing in the standard TOFMS^{27,28} must be modified to account for the resulting field-free drift region h that separates the extraction field E_s from the accelerating field E_d . The total drift time t_{tot} is the sum of the times that an ion spends in each of the four regions (s , h , d , and D), which is given by

$$t_{tot} = \sqrt{2m/q} \left(\frac{s + h/2}{\sqrt{s E_s}} + \frac{\sqrt{s E_s + d E_d} - \sqrt{s E_s}}{E_d} + \frac{D}{2\sqrt{s E_s + d E_d}} \right) \quad (1)$$

First-order space-focusing means that the derivative of t_{tot} with respect to s vanishes at $s = s_0$, which is obtained when

$$D = 2(k_0)^{3/2} \left(s_0 - h/2 - \frac{d}{k_0 + \sqrt{k_0}} \right) \quad (2)$$

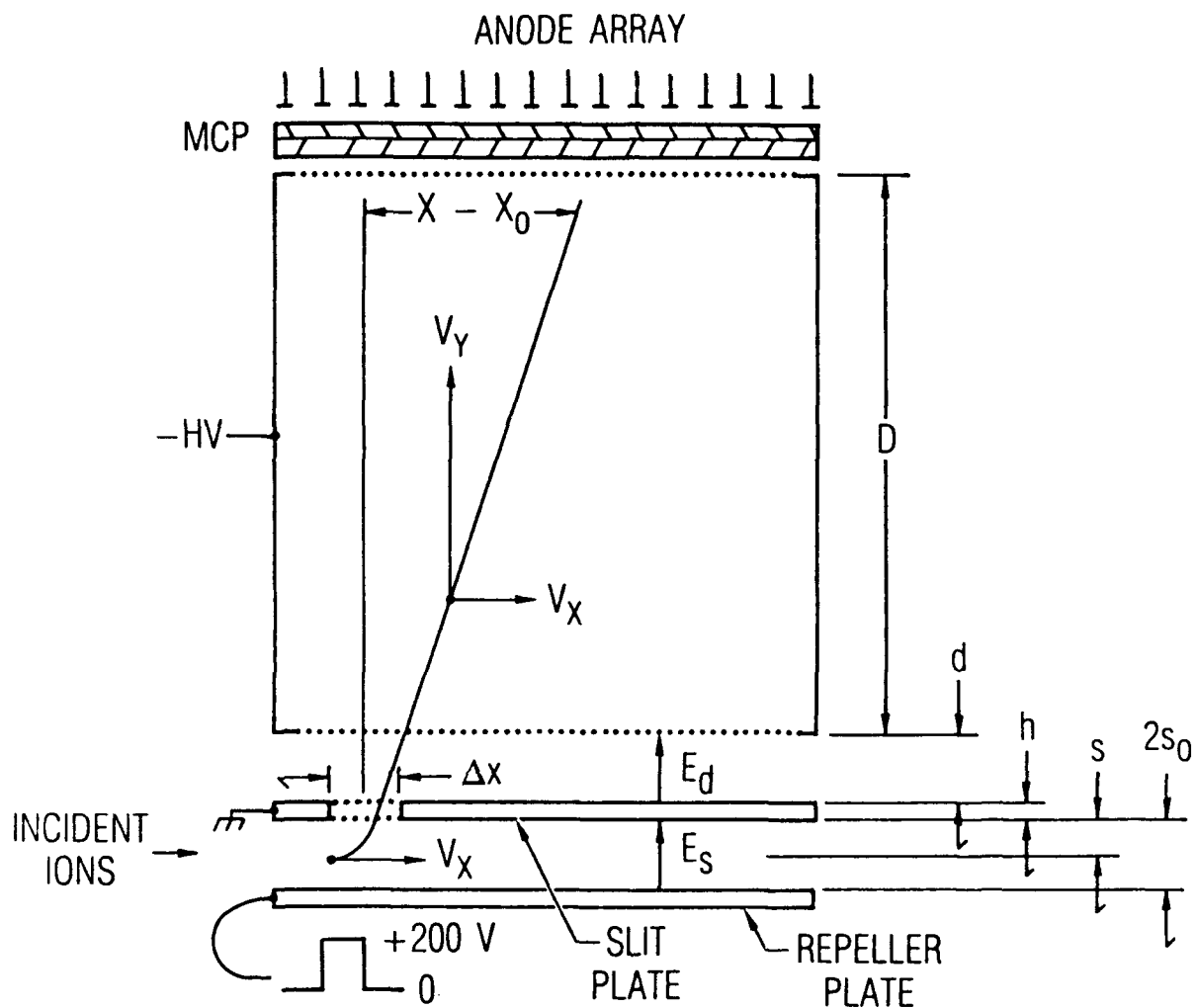


Figure 1. Analyzer Concept and Distance Parameters for Time-of-Flight Mass Spectrometry. Incident ions enter the analyzer and are accelerated by a pulsed electric field toward the position-sensitive detector. Masses are determined by time-of-flight, and energies are determined by displacement along the detector.

$$k_0 \equiv (s_0 E_s + d E_d) / (s_0 E_s) \quad (3)$$

$$U_y \equiv q(s_0 E_s + d E_d) = q k_0 s_0 E_s = (1/2) m v_y^2 \quad (4)$$

Note that a physically meaningful solution to Eq. (2) cannot be obtained if $h \geq 2 s_0$. For convenience the total drift time is rewritten as

$$t_{\text{tot}} = \sqrt{m/2U_y} \left(2\sqrt{k_0} (s_0 + h/2) + \frac{2d\sqrt{k_0}}{\sqrt{k_0} + 1} + D \right) \quad (5)$$

To determine the incident ion energy U_x , we consider the time t_{d+D} that the ion spends traversing the distance between the slit and the detector, which is given by

$$t_{d+D} = \sqrt{m/2U_y} \left(\frac{2d\sqrt{k_0}}{\sqrt{k_0} + 1} + D \right) \quad (6)$$

The displacement along the detector, $x - x_0$, is then

$$x - x_0 = v_x t_{d+D} = \sqrt{U_x/U_y} \left(\frac{2d\sqrt{k_0}}{\sqrt{k_0} + 1} + D \right) \quad (7)$$

where x_0 is the point on the detector corresponding to zero kinetic energy. Equation (7) shows that the displacement for ions at a given incident energy is independent of mass.

The actual values for the TOFMS geometrical parameters in our apparatus are listed in Table 1, and the predicted mass and energy ranges are given in Table 2. The upper limit of the mass range is reached when the extraction time for ions at $s = 2s_0$, given by $t_{2s_0} = \sqrt{4 s_0 m / q E_s}$, exceeds the width of the repeller pulse. Ions that are too heavy to be extracted through the slit before the end of the pulse appear as broadened peaks in the mass spectrum. The accessible energy range is determined by the practical limits for measuring the displacement along the $100 \times 15 \text{ mm}^2$ microchannel plate (MCP). Restricting attention to the range $10 \text{ mm} \leq x - x_0 \leq 90 \text{ mm}$ allows for an adequate cushion at each end of the detector. The highest measurable ion kinetic energy in the present configuration is $U_x = 119 \text{ eV}$, assuming TOFMS space-focusing with a 200 V repeller pulse ($U_y = 2343 \text{ eV}$). The energy range can be extended to $U_x = 500 \text{ eV}$ if the field-free drift distance D is reduced from 391 mm to about 110 mm. However, the time-of-flight analyzer has not yet been tested in this mode.

Table 1. Geometrical Parameters for the Time-of-Flight Mass/Energy Analyzer

$D = 391.1 \text{ mm}$	$\Delta x = 5.08 \text{ mm}$
$d = 5.08 \text{ mm}$	$\text{MCP} = 100 \times 15 \text{ mm}^2$
$h = 1.27 \text{ mm}$	
$s_0 = 2.54 \text{ mm}$	
$k_0 = 23.425$	

$$2\sqrt{k_0}(s_0 + h/2) + 2d\sqrt{k_0}/(\sqrt{k_0} + 1) + D = 430.35 \text{ mm}$$

$$t_{\text{tot}}(\mu\text{s}) = 30.980 \sqrt{M(\text{amu})/U_y(\text{eV})}$$

$$2d\sqrt{k_0}/(\sqrt{k_0} + 1) + D = 399.62 \text{ mm}$$

$$x - x_0 (\text{mm}) = 399.62 \sqrt{U_x/U_y}$$

Table 2. Predicted Mass and Energy Ranges for a Time-of-Flight Analyzer with Geometrical Parameters of Table 1. (The repeller pulse has 1.0 μ s maximum width and amplitudes of 50, 100, and 200 V. The energy limits pertain to displacements along the detector in the range of $10 \leq x-x_0 \leq 90$ mm.)

U_y (eV)	E_S (V/cm)	M^{\max} (amu)	U_x^{\min} (eV)	U_x^{\max} (eV)
585.6	98.4	93.5	0.37	29.7
1171.3	196.9	186.9	0.73	59.4
2342.5	393.7	373.9	1.47	118.8

For the detection of neutral molecules an electron-impact ionizer is added upstream of the ion extraction region. Collision with an electron imparts undesired momentum to the molecule, but the effect is significant only for light species (H_2 , He) at incident energies less than $U_x = 1$ eV. For a rough estimate of the resulting spread in the molecular velocities, consider a head-on elastic collision between an electron with kinetic energy U_e and a molecule of mass M that is initially at rest. The velocity change Δv due to the collision is

$$\Delta v \text{ (km/s)} = 0.651 \sqrt{U_e \text{ (eV)}}/M \text{ (amu)} \quad (8)$$

For example, if $U_e = 70$ eV and $M = 20$ amu we find $\Delta v = 0.27$ km/s, which is about 14% of the velocity expected for the test case of Ne seeded in H_2 with a room temperature supersonic nozzle reported in Section IV.D. Thus, electron-impact ionization places a lower limit on the accessible energy range for neutral molecules. In Section IV.E. other factors that contribute to broadening of the energy spectra beyond the slit-limited resolution are discussed.

Recently, an extensive review was given by Richter and Ho²⁹ of position-sensitive readout schemes for charged-particle detection with MCP electron multipliers. To take full advantage of the rapid cycling capability of the time-of-flight analyzer, a discrete channel position-sensitive MCP detector with a linear array of metal anodes and a separate channel of detection electronics for each anode have been chosen. Presuming that many ions (greater than 10^2) strike the MCP on every cycle of the TOFMS, a complete energy spectrum can be obtained from an analog readout of the charge on each position element of the detector at the time corresponding to the arrival of a particular mass; reading out the detector at multiple times during a TOFMS cycle gives energy spectra for multiple masses. The signals are recorded in fast-analog mode with a gateable current-integrating analog-to-digital converter (ADC) by setting the ADC gate to coincide with the arrival time of the desired mass. Data can be recorded continuously at slow TOFMS cycle rates (less than 0.5 kHz) or in a burst of several hundred cycles at rates as high as 50 kHz (20 μ s time-resolution). In cases where the signal level is low enough that only a few ions strike the detector on each TOFMS cycle, the readout is performed in an ion counting mode using a set of discriminators and gated scalers to sum the counts into mass-resolved energy spectra.

III. CONSTRUCTION

A. VACUUM SYSTEM

The time-of-flight analyzer shown in Figure 2 is housed in a turbo-pumped vacuum chamber suitable for tests with various ionic and neutral beam sources. The analyzer chamber is an 18 x 18 x 12-in.³ stainless steel box with an extension spool on the top face for the ion drift tube and MCP detector. Ports on the other faces of the box are used for feedthroughs and for connections to the turbo-pump and to the beam source chamber. After a mild bake-out the analyzer chamber reaches a base pressure in the 10⁻⁸ torr range as limited by water vapor outgassing. For the measurements reported here the actual background pressure in the unbaked chamber is 2 x 10⁻⁷ torr. The ionizer grid assembly is mounted in the center of the chamber on a tilt table that allows for precise alignment of the accelerating fields with the detector viewing axis. A pulsed electron gun ionizes the incident neutral molecules prior to extraction into the drift tube. A sweeper electric field can be applied upstream of the ionizer to exclude incident charged particles when neutrals are being analyzed.

B. MULTIANODE MCP DETECTOR

The detector is a rectangular MCP (Galileo 3115, 25- μ m-diam pores) coupled to a 96-element array of gold anodes on a Macor substrate, with an array fan-out similar to that described by Gurney, *et al.*³⁰ The anodes are 0.5-mm-wide x 15-mm-long located on 1.0 mm centers. The anodes are used with a chevron MCP with a 100 x 15-mm² active area. To allow for the possibility of detecting either positive or negative ions, the anodes can be floated to high voltages of either polarity while capacitively decoupling the high voltage of the anodes from the low voltage of the preamplifier inputs, as shown in Figure 3. This arrangement also permits the impact energy of the ions on the MCP input face (typically 3.2 keV) to be set independently of the multiplier gain voltage (typically 800 to 900 volts per plate). The 96 bias resistors (1 M Ω , 1/4 W) and decoupling capacitors (1000 pF, 6 kV, ceramic) are arranged on a stack of three circular printed circuit boards that are mounted in the vacuum and supports the anode substrate. The boards are electrically mated by pins and sockets spaced around the perimeter. Standard (nonultra-high-vacuum)

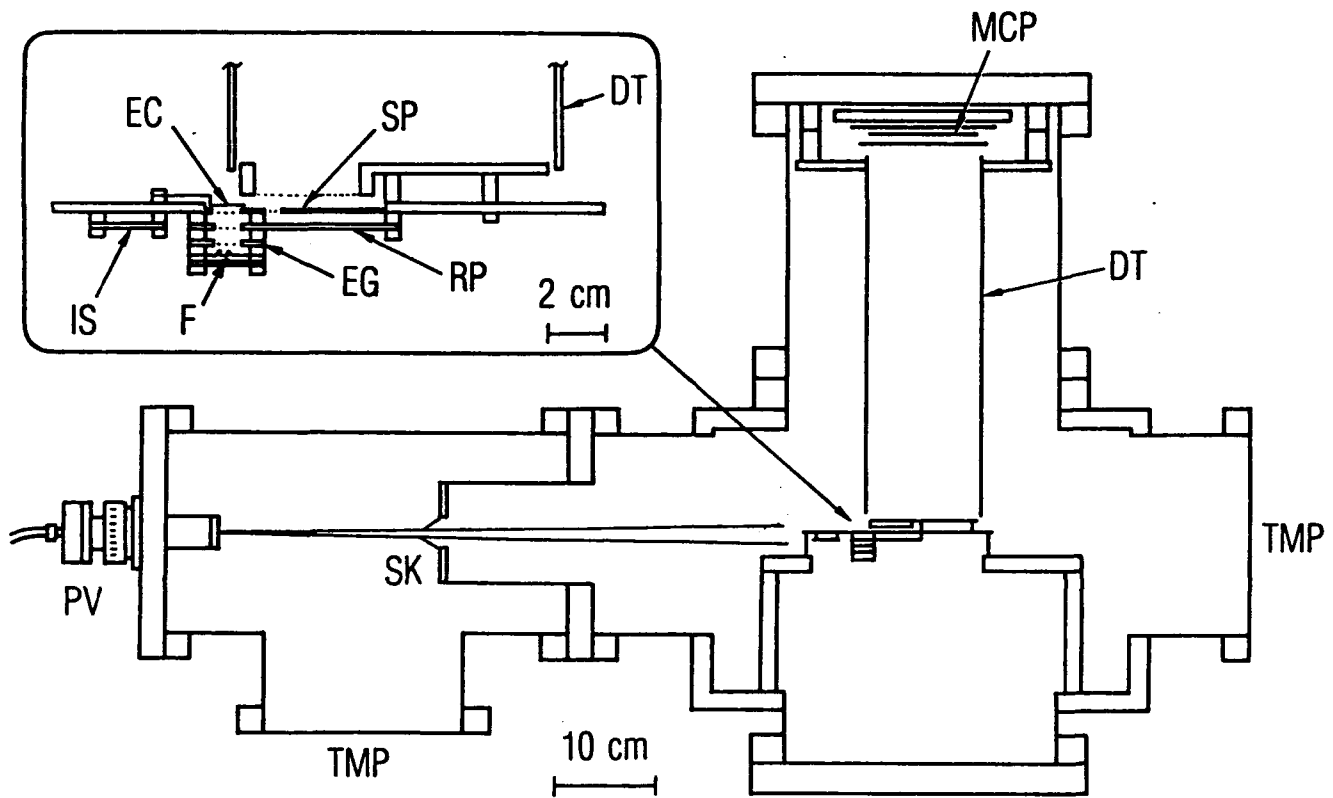


Figure 2. Time-of-Flight Analyzer with Detector Chamber and Differentially Pumped Source Chamber for Tests with Ionic or Neutral Beams. DT = drift tube; EC = electron collector; EG = electron gate; F = filament; IS = ion sweeper; MCP = microchannel plate; PV = pulsed valve; RP = repeller plate; SK = skimmer; SP = slit plate; TMP = turbo-molecular pump.

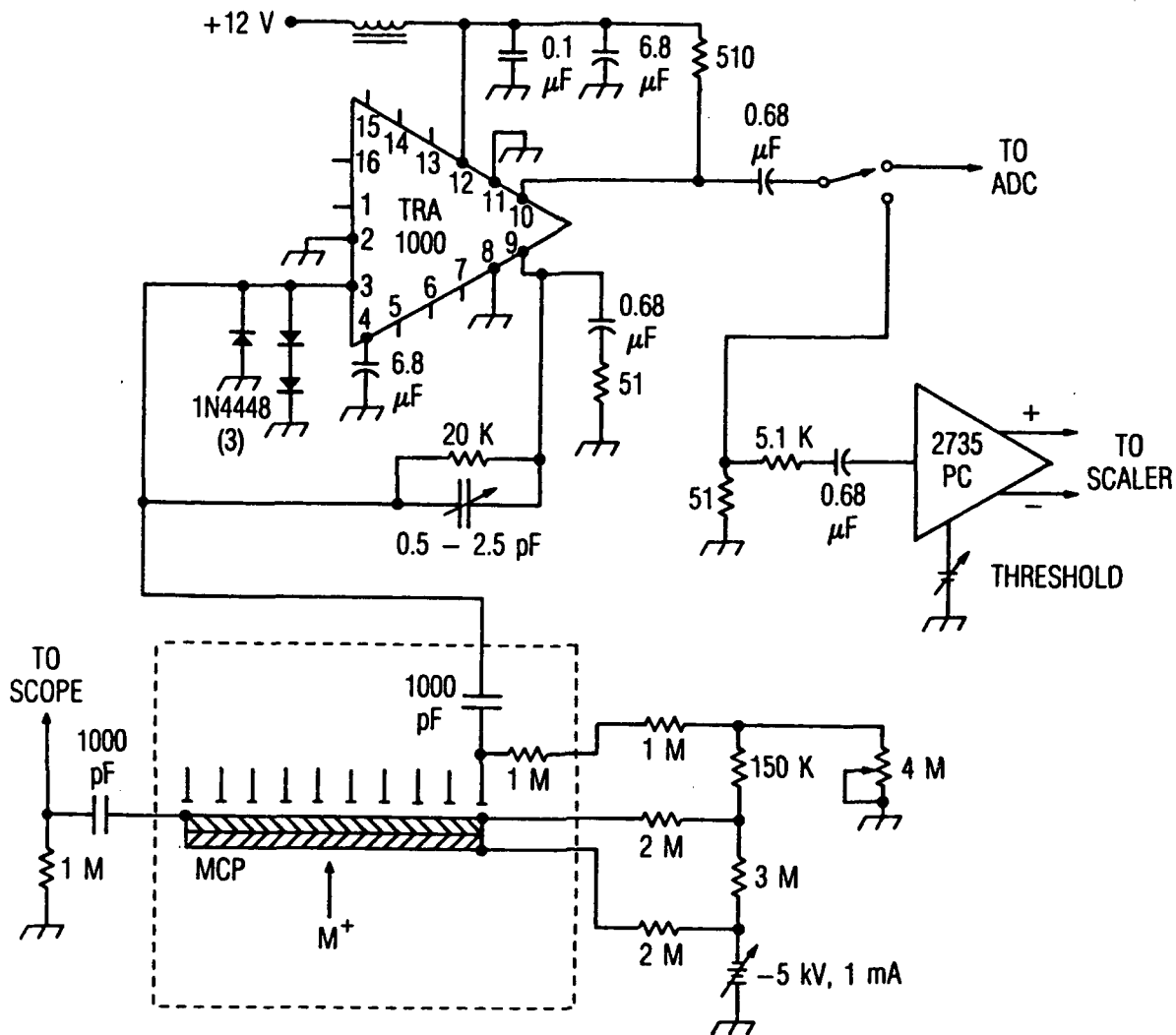


Figure 3. Circuits for the Microchannel Plate Biasing, Signal Decoupling, and Preamplification. The amplified output is recorded by an analog-to-digital converter (ADC) or by a discriminator and scaler. Separate amplification and detection electronics are provided for each of the 96 anodes. The position-integrated signal from the output face of the microchannel plate (MCP) is sent to a digital oscilloscope.

resistors, capacitors, PC boards, and wires are used with tin/lead soldered connections. Placing these components inside the vacuum chamber avoids the need for high voltage signal feedthroughs, although it restricts the detector to rather low bake-out temperatures (70°C has been used with no ill effects). The decoupled signals are fed out through a 13.25-in.-outside diameter mounting flange on four multipin connectors (two 35-pin and two 20-pin). Four high voltage feedthroughs are also included on the flange for connections to MCP input, MCP output, anode bias, and to the grid placed in front of the MCP to shield the ions in the drift region from the voltage on the detector. The components of the multianode MCP detector were designed and fabricated by Galileo Electro-Optics Corporation and assembled and tested in our laboratory.

C. PREAMPLIFIERS

A shielded enclosure for the signal preamplifiers is mounted over the multipin feedthroughs on the detector flange. The 96 amplifiers are arranged on 12 custom PC boards with eight channels for each board. A 15-cm length of RG-174/U coaxial cable connects each feedthrough pin to its corresponding amplifier board, and a 4-m length of RG-174/U conveys each signal from the amplifier output to the 50- Ω terminated ADC or discriminator input. The circuit shown in Figure 3 uses the LeCroy (LeC) TRA1000 amplifier chip to linearly amplify the anode charge to a level that is suitable for input to the ADC defined on p. 16. The linearity of the amplifier/ADC system has been tested with calibrated input charge pulses containing between 0.005 and 1.3 pC and having widths from 4 to 64 ns full-width at half maximum (FWHM). The average charge gain is $Q_{out}/Q_{in} = 3.3 \times 10^2$, with random deviations from this value that are no worse than $\pm 7\%$ over the entire range of inputs tested. For narrow input pulses (4 ns FWHM) the amplifier output pulse width is 31 ns FWHM; for wide input pulses the output rise time is 41 ns (10% to 90%). The full scale output into 50 Ω is -1.0 V with a noise level of less than 2 mV p-p (125 MHz bandwidth). Matching the response of all 96 circuits to within a $\pm 2\%$ range is achieved by adjusting the feedback trim capacitor while comparing the output of the amplifier to a standardized waveform. If the MCP is operated at a charge gain of 1×10^6 , a single ion striking the detector presents 0.16 pC to the anode and becomes 53 pC after preamplification. The overall gain is sufficient for single-ion hits to be cleanly registered by the 11-bit ADC,

which has a sensitivity of 0.25 pC/count and a full scale of 480 pC. The required gain, linearity, channel-to-channel uniformity, and low noise are achieved at the expense of the rise time, which ultimately limits the mass resolution. Other factors affecting the observed mass resolution are considered in Section IV.E.

D. FAST-ANALOG ELECTRONICS

The configuration of the data collection electronics for fast-analog detection is shown in Figure 4. The heart of the system is the 96-channel gated ADC (LeC 4300B, six modules) with an ECL-bus driver module (LeC 4301) and a 32K-word buffer memory (LeC 4302, two modules). The ADC is housed in a CAMAC crate along with a clock generator (LeC 8501) for timing the burst of readout cycles and a high voltage power supply (LeC 2415) for the MCP and anodes. A crate controller (Transiac 6001) provides the interface to an 80286-based laboratory computer. An adjacent NIM bin contains a second clock generator (BNC 8010, two modules) and eight independent gate/delay and logic translation channels (Phillips 794 (two modules), Phillips 711, and LeC 4616). Six of these channels are used for gating the ADC modules via ECL logic, and the remaining two are used to trigger the electron beam pulser (HP 214B) and the ion repeller pulser (Avtech AVR-A-1-AS2) via TTL logic. A 125-MHz digital oscilloscope (LeC 9400) records the analog "sum" signal from the position-sensitive detector via pick-off from the output face of the MCP, as shown in Figure 3. This gives a convenient record of the position-integrated TOFMS waveform for the purposes of tune-up and mass identification. The scope also records a logic "sum" signal from the gate/delay modules to facilitate adjusting the ADC gates to coincide with the mass peaks of interest. The scope may be triggered through a rate divider (Ortec RD2000) at some chosen fraction of the ADC burst rate to permit a sequential recording of digitized mass spectra at representative intervals during a long burst.

The ADC is given gate pulses of 100 to 400 ns width and digitizes the charge received during the gate to 11 bits in 9.0 μ s. The 96 words of ADC data must be transferred to the buffer memory before a new digitization is initiated. Transfer over the ECL-bus requires 10.8 μ s and begins within 0.2 μ s after the digitization is complete. Thus, the fast-analog electronics can be interrogated once every 20 μ s for a maximum burst-mode sampling rate of

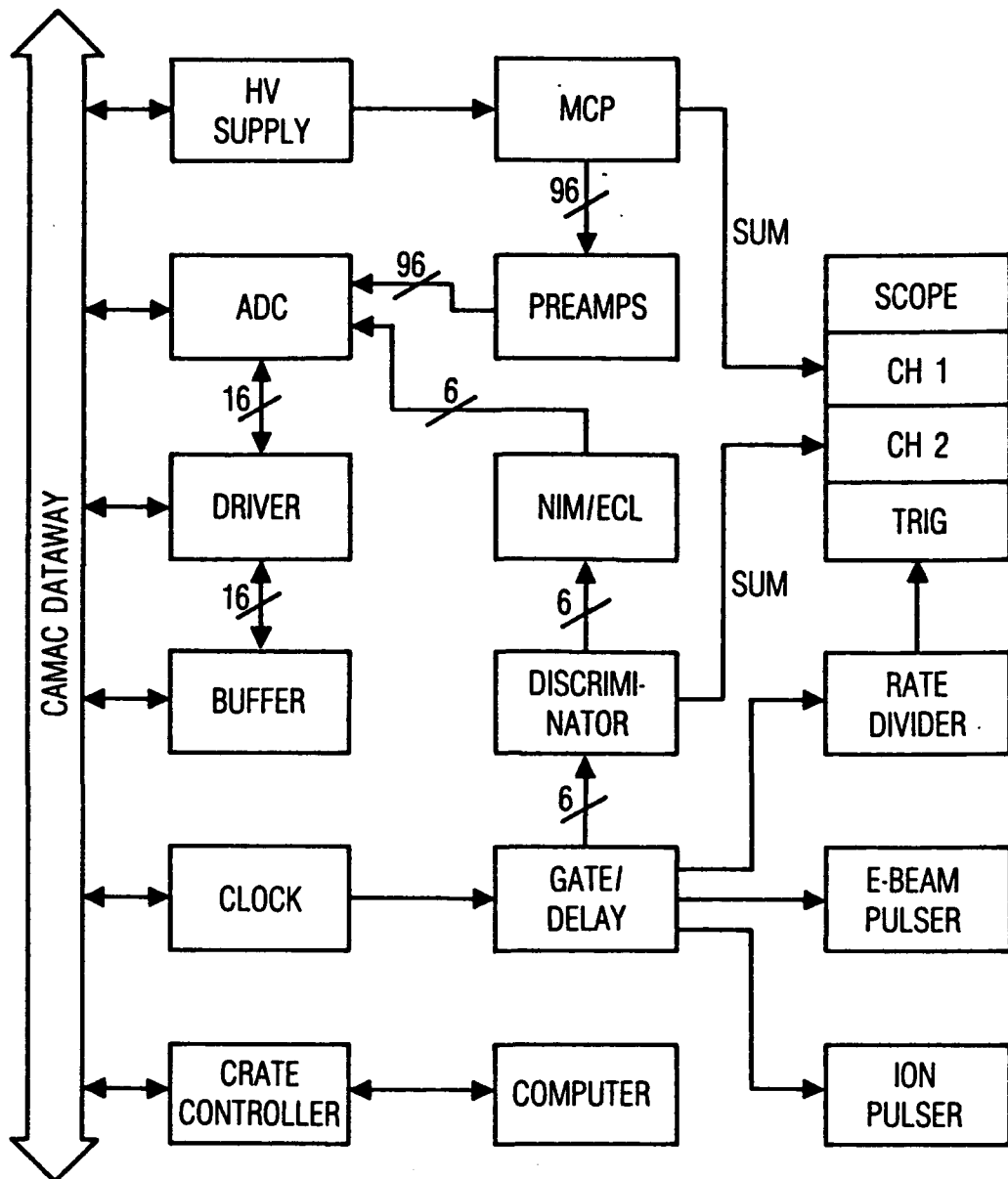


Figure 4. Data Collection Electronics for the Time-of-Flight Analyzer in the Fast-Analog Mode of Detection. A burst of clock cycles triggers the pulse generators for the electron gate, ion repeller, and ADC gates. The oscilloscope records the position-integrated TOFMS waveform and the ADC gate intervals.

50 kHz. The cycling of the TOFMS (pulsing of the grids followed by ion drift) proceeds at the same time as the digitization and transfer of the signals from the previous cycle. Reduced sampling rates are necessary if the time from the start of the electron gate pulse to the arrival of the heaviest ion at the detector exceeds 20 μ s. (This is the reason for using a rate of 40 kHz when detecting neutral beams of Kr seeded in H₂ as reported in Section IV.D.) The 32K-word storage capacity of the buffer memory allows for a burst of up to 341 consecutive readouts of the detector before data transfer to the computer is required. The memory can be expanded by the addition of more LeC 4302 modules.

The 96 available detector elements are partitioned between mass and energy channels to match the requirements of a given experiment. Energy spectra for multiple masses are recorded using an anode interleaving scheme that relies on gating the ADC at the module level, meaning 16 channels at a time. The first ADC module (designated A) reads out anodes 1,7,13,...,91; the second module (B) reads out anodes 2,8,14,...,92; continuing up through the sixth module (F), which reads out anodes 6,12,18,...,96. For sampling six separate masses, the ADC modules are gated in the sequence A, B, C, D, E, F; for sampling three masses the sequence is A+D, B+E, C+F; for sampling two masses, the sequence is A+C+E, B+D+F; for sampling a single mass, all six modules are gated simultaneously. This interleaving method ensures that the energy spectra are recorded in equally spaced detector elements whether the number of masses being sampled is six, three, two, or one.

E. ION-COUNTING ELECTRONICS

For situations when only a few ions strike the detector on each TOFMS cycle, it may be more appropriate to operate in an ion counting mode rather than with analog detection. In this case the 96 preamplified signals are routed to a set of discriminators (LeC 2735PC, six cards in a home-built enclosure) and 20 MHz scalars (LeC 4434, three CAMAC modules). The 2735PC is a 16-channel time-over-threshold discriminator triggerable by current pulses in the range of 2 to 20 μ A with widths as short as 8 ns. The unamplified MCP anode pulses from single-ion hits can easily reach peak currents in this range, but they are too narrow (less than 5 ns) for reliable operation with the scalars that require 15 ns minimum width ECL logic pulses. The TRA1000

preamplifier output pulses are well matched to the scaler pulse width requirements, so these signals are routed to the discriminators via 100:1 attenuators, as shown in Figure 3. The three 32-channel scaler modules can be independently gated (by fast VETO inputs) to record energy spectra for three different masses by the anode interleaving scheme as previously described.

One limitation of this MCP detector is that the pulse height distribution is not optimized for ion counting. Rather than trying to achieve gain saturation (as appropriate for operation with a discriminator) our primary objective is to maximize the dynamic range of the signal for analog detection. For this reason, 50- μm -thick shims are inserted between the two plates in the chevron instead of using a close-coupled mounting arrangement. The gap between the plates enhances the spreading of the first-stage output charge over many microchannels at the second stage input, yielding better analog response with little or no gain saturation. This precludes one of the normal benefits of ion counting, because there is no definitive way of setting the discriminator threshold to optimize the signal-to-noise ratio, as would be the case with a gain-saturated pulse height distribution. The increased sensitivity achieved by ion counting also comes at the expense of time-resolution. Although the duty factors for the electron gate and ion repeller pulse generators permit a burst-mode cycling rate of up to 50 kHz, the rate must be reduced to 5 kHz for continuous operation in ion counting. This is sufficient for mass-resolved energy spectra to be accumulated within a period of a few seconds.

IV. PERFORMANCE

A. GAIN VS. POSITION

Previous work with multianode MCP detectors has shown that there can be large variations in gain as a function of position along the detector.³⁰⁻³² One approach that we have used to evaluate this effect is to illuminate the MCP in a pseudouniform manner with a diffuse, low-energy electron or ion beam for a direct estimate of the position dependence of the gain. Alternatively, a collimated ion beam is scanned across the MCP while recording the signal at various positions. Typical results for the gain vs. position are shown in Figure 5. The spatial variation of the gain measured with the scanned beam is relatively small ($\pm 15\%$) and is amenable to correction with normalizing software. Superimposed on this coarse variation are random channel-to-channel fluctuations of $\pm 10\%$ that we have not attempted to quantify thus far. The diffuse beam results show an overall variation of $\pm 35\%$, but we attribute some of the "excess" signal observed near the ends of the detector to ions scattered from the wall of the drift tube. The observed spatial dependence of the detector response is attributed primarily to nonuniform MCP gain, since the preamplifiers and detection electronics are known to be matched to within better than $\pm 5\%$. A possible cause of nonuniformity is variation of the inter-stage gap-width (nominally 50 μm) due to bending of the plates when held by retaining clips at either end.³²

B. CROSS-TALK

Cross-talk between channels is another important issue for multianode MCP detectors.²⁹⁻³¹ We have measured the analog cross-talk in bench-top tests by applying a simulated signal to one anode and monitoring the amplified output of nearby channels. The magnitude of the pickup at the adjacent channel is about 9% of the applied signal, dropping to 5% and then 3% as one takes successive steps away from the signal source. We can estimate an upper limit to the cross-talk in the ion counting mode by directing a low-intensity ion beam at the detector and comparing the number of true single-channel hits to the number of events where two hits appear in adjacent channels. This test shows that the ion counting cross-talk in adjacent channels is certainly less than 8% for typical multiplier gain and discriminator settings. Several features

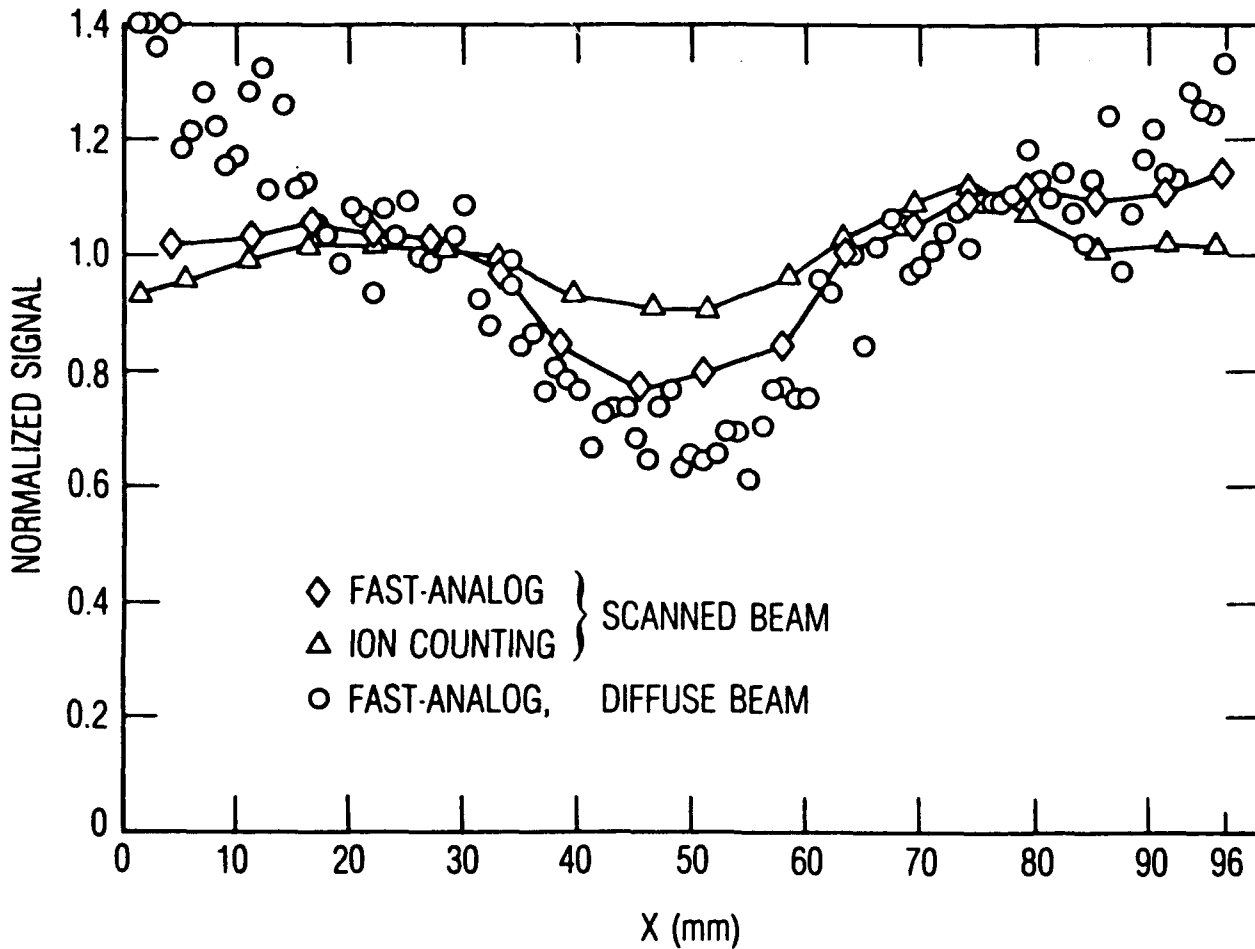


Figure 5. Spatial Dependence of the Detector Response as Measured with a Scanned, Collimated Ion Beam and with a Diffuse, Pseudouniform Ion Beam. The multiplier is set to 825 V/plate in fast-analog mode and 875 V/plate in ion counting. No "dead" detector channels are observed.

of the analyzer design tend to minimize cross-talk difficulties. The pre-amplifier circuit with its low input impedance (ca. 3 Ω) and relatively slow rise-time (41 ns) helps to overcome the pickup due to channel-to-channel capacitance. Moreover, the anode interleaving scheme for detecting multiple masses results in the adjacent anodes being read out at different times during the TOFMS cycle, thus reducing the cross-talk to a negligible level in these cases.

C. ION BEAMS

The simplest mode of operation for the time-of-flight analyzer is the detection of ions produced by an external source. For test purposes we install a home-built ion gun in the differentially pumped source chamber and use it to generate continuous Ar^+ beams with 5 to 150 eV kinetic energy. The energy spread is expected to be ± 0.5 eV due to the potential drop across the region where the ions are formed. The ionizing electron current in the gun is set below the point where electron space-charge perturbations have an obvious effect on the ion energy (as measured by the time-of-flight analyzer). Calibration of the energy and intensity of the ion gun using an electrostatic deflection analyzer is planned for a later stage of the project.

The TOFMS cycle is initiated by applying a repeller pulse having an amplitude of 50 to 200 V and a width of 1.0 μs . The duration and amplitude are sufficient for all of the 40-amu ions in the extraction region to pass through the slit before the end of the pulse. The drift tube voltage and the repeller pulse amplitude are set to the values predicted for space-focusing (e.g., $s_0 E_s = 50$ V, $d E_d = 1121$ V, $U_y = 1171$ eV). Adjusting the voltages in either direction while monitoring the width of a mass peak shows the desired space-focusing behavior at the predicted voltage settings. Also, the measured TOFMS drift times agree with values predicted by Eq. (5) to within $\pm 1\%$. The TOFMS is cycled continuously at 5 kHz, and data are recorded by gated ion counting on the Ar^+ peak, typically summing the counts over a dwell interval of 10 s before storing a spectrum.

Figure 6 shows a set of spectra taken at $U_y = 1171$ eV with nominal ion beam energies (U_x) from 10 to 45 eV. These data provide a means for calibrating the energy scale and the zero offset of the analyzer. By determining the position of the centroid of each peak in Figure 6 and plotting these values

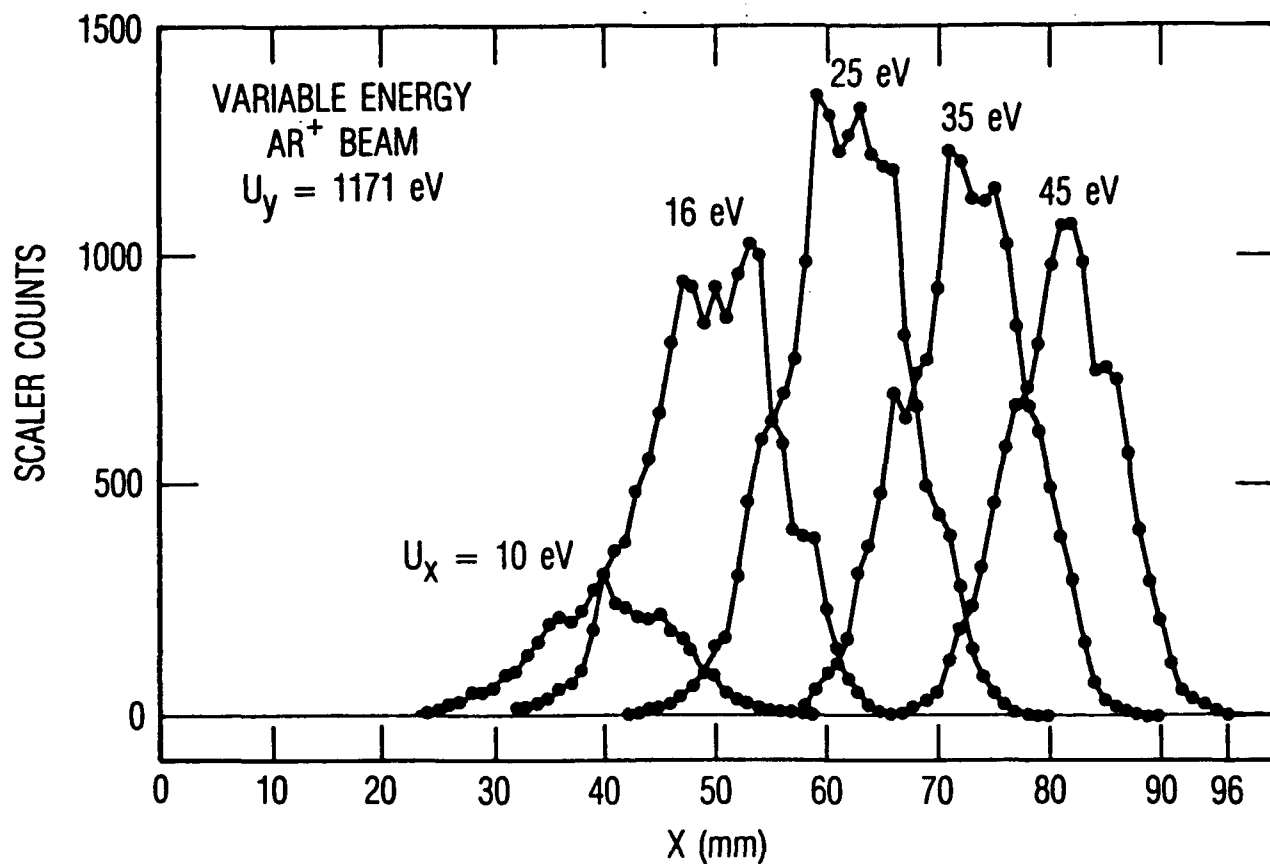


Figure 6. Position-Sensitive Detector Output for Ar⁺ Beams with Nominal Kinetic Energies Between 10 and 45 eV Recorded by Ion Counting Detection at $U_y = 1171$ eV. The observed peak positions are used for calibration of the energy scale as shown in Figure 7. The variation in intensity at the different energies is attributed primarily to the ion source, but may also reflect changes in the analyzer transmission function.

against $\sqrt{U_x}$, we obtain the plot shown in Figure 7 along with results for three other values of U_y . Using Eq. (7), a linear regression on each of the data sets yields an average zero offset of $x_0 = 2.7 \pm 0.6$ mm. For $U_y = 586$ and 1171 eV the least-squares slopes are in excellent agreement (better than 1%) with the values predicted by Eq. (7). For $U_y = 2343$ and 3146 eV the slopes exceed the predicted values by 5 and 7%, respectively, and systematic deviations from linearity are evident. Although electrostatic shielding is used to prevent the incident ions from being adversely affected by the high voltage of the drift tube, more shielding may be needed to resolve this issue. Field distortions near grid wires may also be playing a role in this case (refer to Section IV.E.).

D. NEUTRAL BEAMS

Testing the analyzer with neutral beams is accomplished by installing a pulsed molecular beam valve (Newport BV-100) in the source chamber in place of the ion gun. Although the pulsed nozzle is operated only at ambient temperature (294 K), we can still obtain neutral particles with suitable kinetic energies using the seeded beam method. The gas mixture in these tests is 1% Kr + 4% Ne + 95% H₂ (mean molecular weight = 3.56 amu), expanded from 3 atm through a 0.5-mm-diam orifice. For an ideal isentropic expansion^{33,34} these conditions are expected to yield a terminal velocity of 2.01 km/s for all three species, corresponding to $U_x = 0.42$ eV for Ne and $U_x = 1.75$ eV for Kr. The actual energies are probably somewhat less than these values due to slippage in the expansion.

The pulsed electron gun used for detecting neutral beams must be carefully adjusted to avoid perturbing the energies of the particles being analyzed. The electron impact energy is set no higher than 70 eV in order to minimize the momentum transfer to the ion, as discussed in Section I. For low-energy neutrals, the sensitivity of the analyzer is limited by the restriction to rather low electron beam currents. If the electron current density is too high (greater than 200 $\mu\text{A}/\text{cm}^2$), significant shifts are observed in the Ne and Kr energy spectra due to retardation of the ions by the electron space charge. The delay between the 5- μs -wide electron gate pulse and ion repeller pulse must be adjusted to allow the ions time to drift downstream approximately 15 mm from the ionization region to the extraction region. For

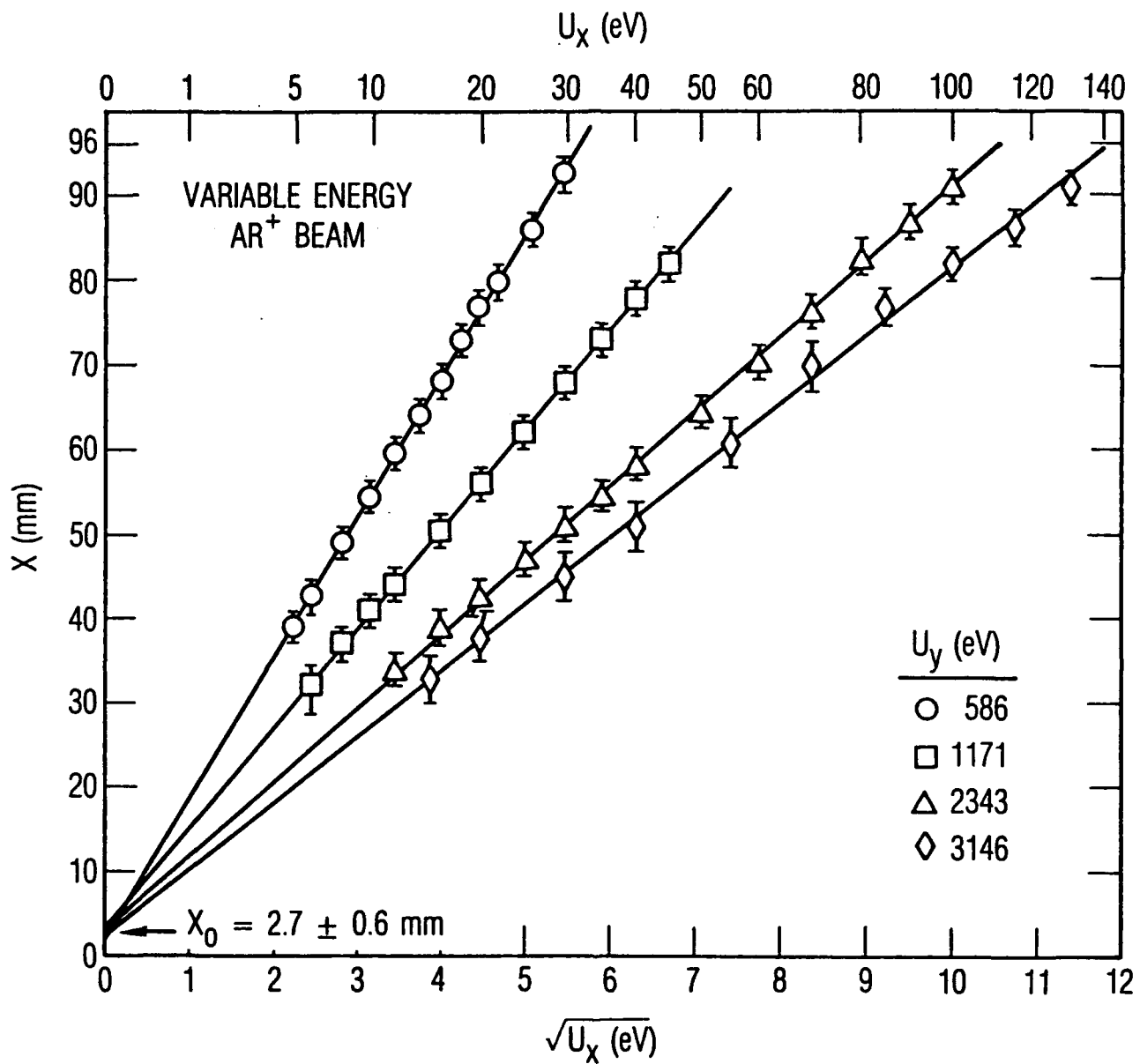


Figure 7. Energy Calibration Data for Ar⁺ Beams with Four Different TOFMS Drift Energies U_y . The position of the peak centroid, x , is plotted against the square root of the Ar⁺ energy, $\sqrt{U_x}$. The average value of the least-squares intercepts is $x_0 = 2.7 \pm 0.6$ mm, which gives the zero offset of the energy scale. TOFMS space-focusing is degraded at $U_y = 3146$ due to the 200 V amplitude limit of the repeller pulse generator.

Ne and Kr seeded in H₂ the ion repeller pulse is delayed by 9 to 12 μs after the leading edge of the electron gate for optimum transmission. This delay is consistent with the time required for ions to drift 15 mm at 2 km/s, namely 7.5 μs. In principle one could avoid the need for this delay adjustment by running with a continuous electron beam, but this produces a significant number of non-time-correlated ion counts that are suppressed by pulsing the electron beam.

Figure 8 shows typical mass and energy spectra for Ne and Kr sampled near the peak of a gas pulse having a duration of 450 μs. The mass resolution is sufficient to separate the adjacent peaks corresponding to ⁸²Kr, ⁸³Kr, and ⁸⁴Kr. The width of the ⁸⁴Kr peak is 43 ns FWHM prior to amplification and 46 ns FWHM at the output of the preamplifiers, which is consistent with unit mass resolution to above 100 amu. Figure 8 also shows the 140-ns-duration ADC gate pulses adjusted to coincide with the ²⁰Ne and ⁸⁴Kr mass peaks, along with the resulting energy spectra averaged over 20 gas pulses. The raw output from the position-sensitive detector gives the number density distribution $N(\sqrt{U_x})$, where $N(\sqrt{U_x})d\sqrt{U_x}$ is the number of molecules per unit volume between $\sqrt{U_x}$ and $\sqrt{U_x} + d\sqrt{U_x}$. We obtain the flux distribution $I(U_x)$ by first multiplying $N(\sqrt{U_x})$ by the velocity v_x to convert from number density to flux and then transforming with the appropriate Jacobian, as follows:

$$I(U_x) = v_x N(\sqrt{U_x}) |d\sqrt{U_x}/dU_x| \propto N(\sqrt{U_x}) \quad (9)$$

The quantity $I(U_x)dU_x$ is the number of molecules per unit area per unit time with energies between U_x and $U_x + dU_x$. According to Eq. (9), a normalized plot of $N(\sqrt{U_x})$ vs. U_x is equivalent to a normalized plot of the flux distribution as a function of energy. The observed energy spectrum for ⁸⁴Kr in Figure 8 shows a maximum at $U_x = 2.0$ eV, in fair agreement with the energy of 1.75 eV predicted for this gas mixture. The ²⁰Ne spectrum has its maximum at $U_x = 0.8$ eV, as compared with the predicted energy of 0.42 eV. These energy shifts seen for low-energy neutrals are due either to electron space-charge perturbations, to collisional effects in the ionization region, or to a sharp decline in the analyzer transmission at low energy. The ²⁰Ne results are at the lower limit of the energy range accessible to the analyzer.

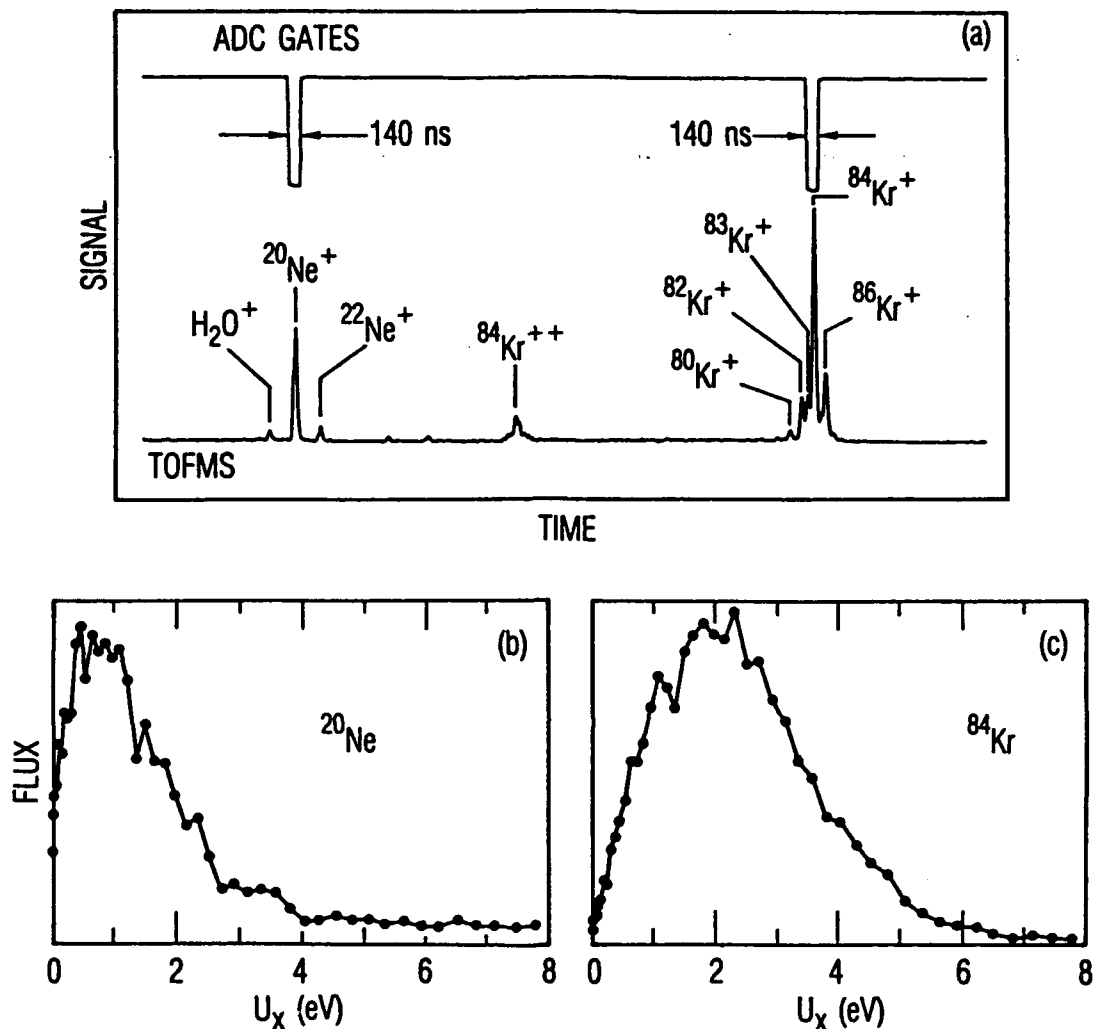


Figure 8. (a) Position-Integrated TOFMS Waveform for a Pulsed Neutral Beam Containing Ne and Kr Seeded in H_2 Using $U_y = 586$ eV, as Measured near the peak of a 450- μs -duration gas pulse. The ADC gates coincide with the arrival of the ^{20}Ne and ^{84}Kr mass peaks. (b),(c) Kinetic energy spectra for ^{20}Ne and ^{84}Kr using the gated ADC and averaging over 20 gas pulses. The apparent flux for ^{20}Ne above 4 eV is an artifact of the ADC zero offset.

The time-resolving capability of the analyzer is explored by taking multiple readouts over the duration of a single gas pulse. Figure 9 shows such a sequence of TOFMS waveforms along with a record of the non-mass-selected ion current obtained by operating the detector as a fast ionization gauge.²⁸ Using a burst rate of 40 kHz yields 18 mass and energy spectra during the course of a 450 μ s gas pulse. The energy spectra for ^{84}Kr from the pulsed neutral beam recorded in burst mode are shown in Figure 10. The time-resolution is sufficient to detect the intensity variations within the gas pulse due presumably to scattering of the directed flow by the transient pressure build-up in the beam source chamber. The data shown here are averaged over 20 gas pulses to improve the signal-to-noise ratio, although in principle the same information could be obtained for a single pulse if the neutral beam had somewhat greater intensity. In this test the estimated number density of Ne or Kr at the ionizer is in the 10^{10} cm^{-3} range. The observed signal levels suggest that low-energy neutral beams could be readily detected down to the 10^9 cm^{-3} range by fast-analog readout and to the 10^8 cm^{-3} range by ion counting. Neutral particles at higher energies can be detected with improved sensitivity by increasing the electron beam current.

E. RESOLUTION

In principle the energy resolution is governed by the width of the defining slit, $\Delta x = 5 \text{ mm}$, shown in Figure 1. None of the spectra we have measured for either ionic or neutral beams shows a FWHM less than about 12 mm in the raw data from the position-sensitive detector. For low-energy neutrals there are the possibilities of broadening caused by momentum transfer with the ionizing electron and space-charge effects. Detector cross-talk or stray electric and magnetic fields also could be broadening the energy spectra for both ions and neutrals. It appears, however, that the major portion of the observed energy spread is caused by field distortions near the grid wires covering the slit. Figure 11 shows a set of Ar^+ trajectories calculated on a two-dimensional potential that matches our present configuration, revealing substantial deflections depending on where the ions pass through the gaps between the wires. Trajectories that initially were parallel are seen to diverge after passing through the grid. The magnitude of this effect was not recognized until after completion of the measurements reported here. We plan to replace the existing 70 lines-per-inch, 90%-transmitting copper mesh with a

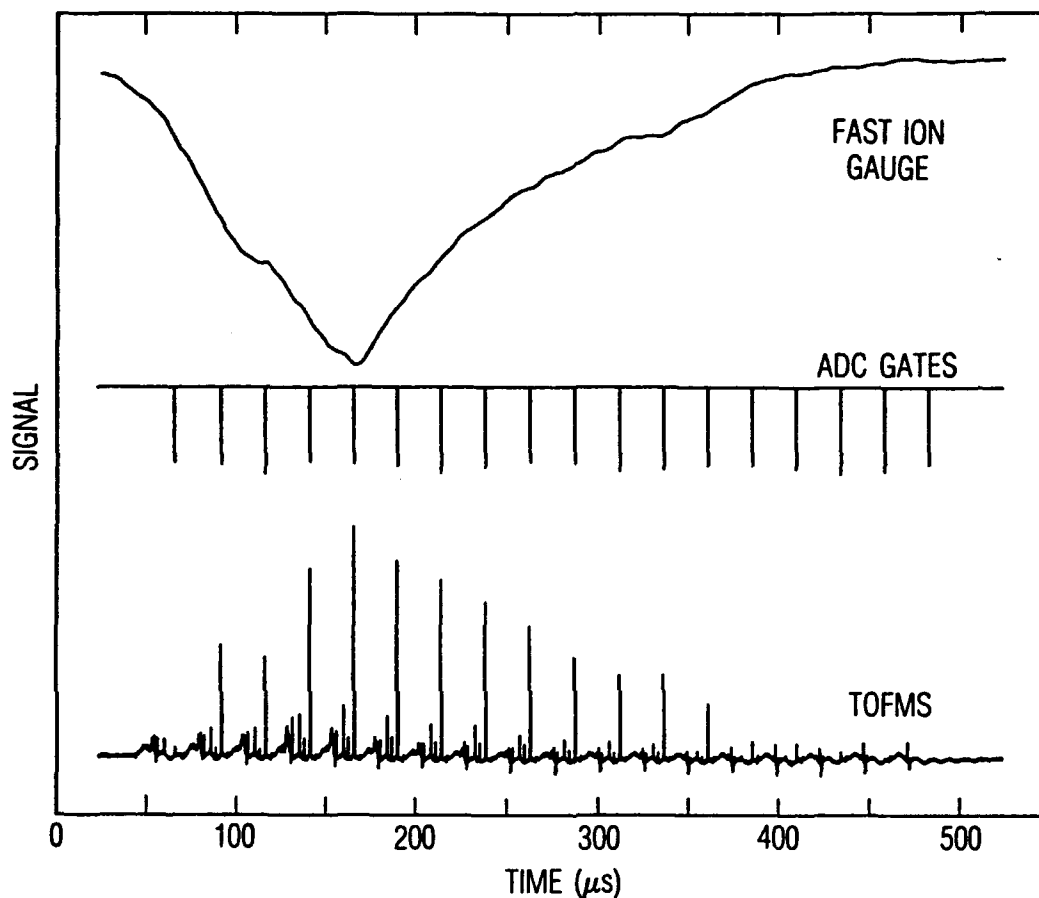


Figure 9. Sequential TOFMS Waveform Taken with a 40 kHz Burst Rate During a Gas Pulse Containing Ne and Kr Seeded in H_2 Under Conditions of Figure 8. The lower trace is the position-integrated output from the microchannel plate during the burst of 18 TOFMS cycles. The middle trace shows the ADC gate coinciding with the ^{84}Kr peak on each cycle. The upper trace is a negative-going signal showing the total ion current when the ionizer and microchannel plate are used as a fast ionization gauge.

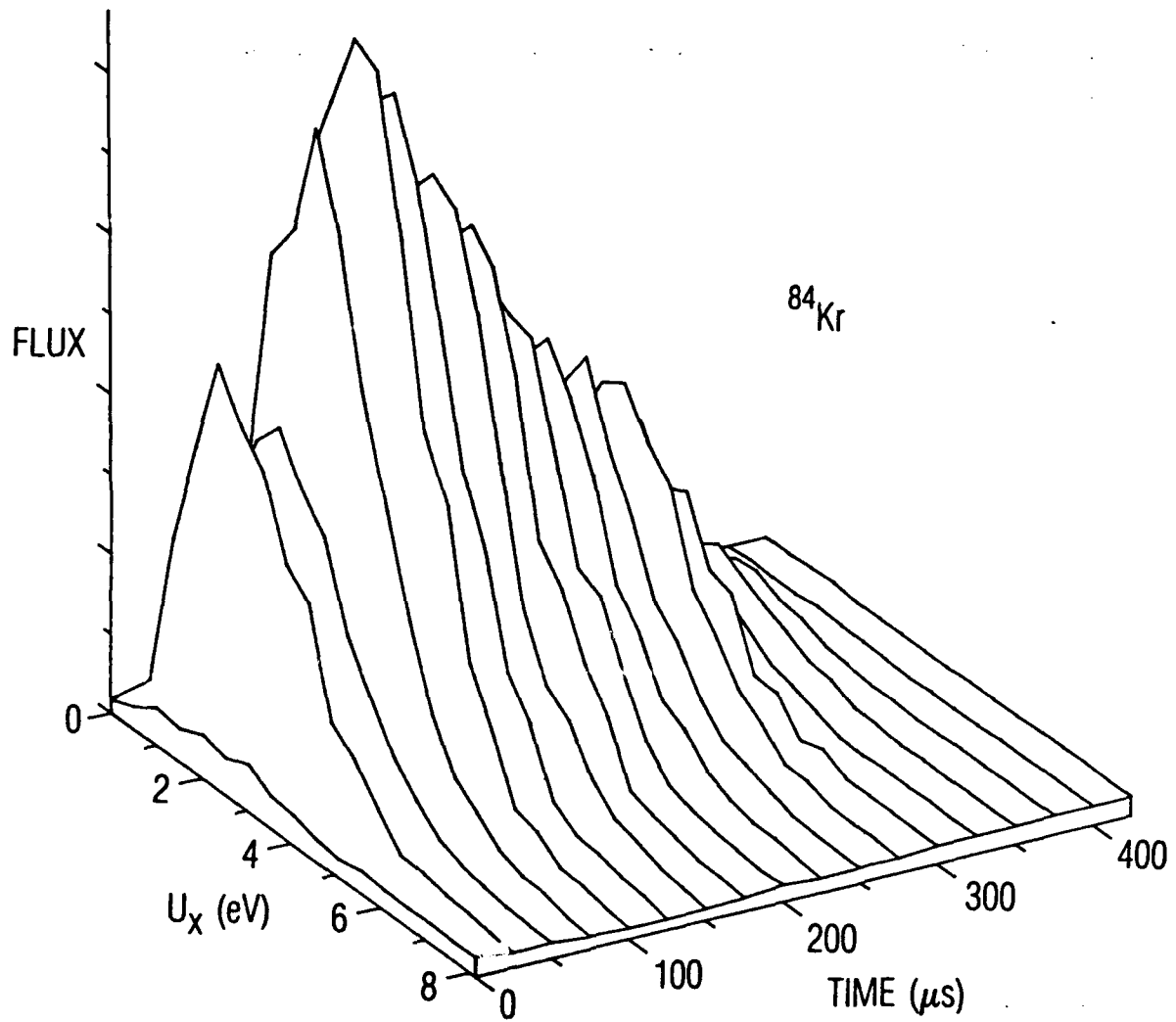


Figure 10. Time-Resolved Energy Spectra for ^{84}Kr Recorded at 25 μs Intervals Under Conditions of Figure 9. The results are an average over 20 gas pulses.

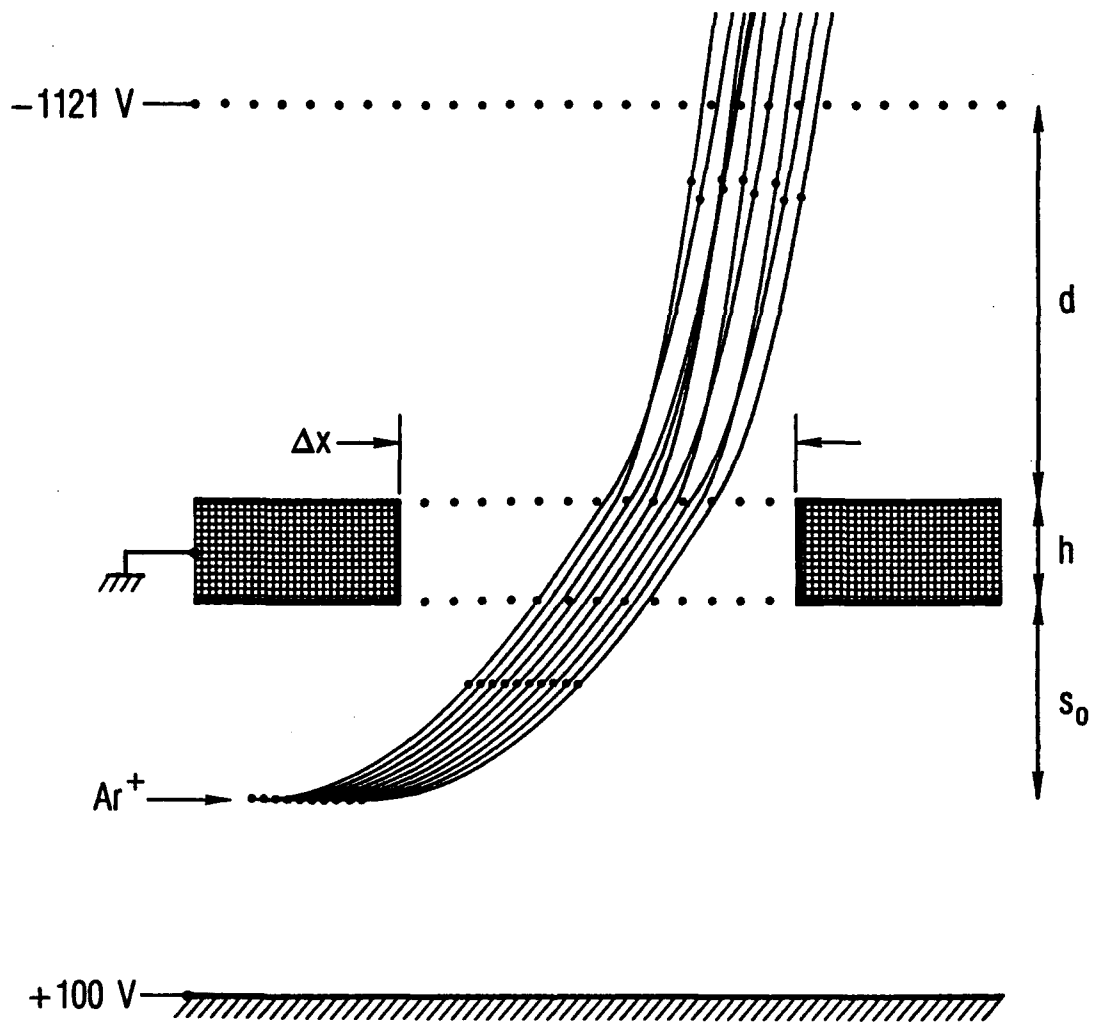


Figure 11. Calculated Ion Trajectories Showing Deflection by Field Distortions Near the Grid Wires Covering the Slit in the Mass/Energy Analyzer. The electric potential is calculated in two dimensions only. Trajectories are for Ar^+ with $U_x = 25$ eV and $U_y = 1171$ eV. Time-marker dots are shown at intervals of $0.25 \mu s$. Field distortions are a significant source of broadening in the observed mass and energy spectra.

more finely spaced one to alleviate the field distortion problem. It should be sufficient to replace only the grid that separates region h from region d in Figure 11.

A recent analysis by Bergmann, *et al.*³⁵ predicts the observed broadening of our energy spectra caused by field distortions near the grid wires. Translating Eq. (30) of Ref. 35 to suit the present case, we express the FWHM spread in the analyzed velocity v_x for ions passing from region h to region d as

$$\Delta v_x \approx a q E_d / 4m v_h = (a/4d)(k_0 - 1) \sqrt{q s_0 E_s / 2m}, \quad (10)$$

where a is the mesh spacing, and $v_h = \sqrt{2q s_0 E_s / m}$ is the velocity in region h for ions originating at $s = s_0$. In the case when $s_0 E_s = 50$ V ($U_y = 1171$ eV), $a = 0.363$ mm (70 lines-per-inch), and $M = 40$ amu (Ar^+), we obtain $\Delta v_x = 3.11$ km/s. For the data shown in Figure 6, the drift time for Ar^+ is $t_{d+D} = 5.32$ μ s, which results in a predicted spread across the detector of $\Delta v_x t_{d+D} = 16.5$ mm. The observed FWHM of the peaks in Figure 6 is about 15 mm, in good agreement with the calculated value. A similar analysis helps to explain the peak widths in the time-of-flight mass spectrum. The arrival time of an ion at the detector depends on how much deflection occurs at the grid, as demonstrated by the time-marker dots in Figure 11. The FWHM spread in the drift velocity v_y due to the grid is

$$\Delta v_y \approx (1/2) \left(v_h - \sqrt{v_h^2 - (\Delta v_x / 2)^2} \right) \quad (11)$$

Recalling from Eq. (4) that $v_y = \sqrt{2k_0 q s_0 E_s / m}$, we find that the relative width of the TOFMS peak is

$$\Delta t / t = \Delta v_y / v_y = \left(1 - \sqrt{1 - (a/8d)^2 (k_0 - 1)^2} \right) / (2 \sqrt{k_0}) = 2.1 \times 10^{-3} \quad (12)$$

For the data shown in Figure 8, the drift time for $^{84}\text{Kr}^+$ is $t_{\text{tot}} = 11.73$ μ s and the peak width (FWHM) prior to amplification is 43 ns, for an observed spread of $\Delta t / t = 3.7 \times 10^{-3}$. Field distortion apparently is the source of most of the broadening, but several other sources also may be contributing. A

direct calculation of the arrival time distribution for first-order space-focusing with a uniform number density of ions across the extraction region provides an intrinsic peak width of $\Delta t/t \approx 1 \times 10^{-4}$. Electron-impact ionization imparts a velocity spread that could be as large as $\Delta v_y/v_y \approx 1.8 \times 10^{-3}$ based on Eq. (8). The angular acceptance of the analyzer ($\pm 0.3^\circ$) and the resulting beam divergence lead to a velocity spread of $\Delta v_y/v_y \approx 5 \times 10^{-4}$. Folding these contributions together with the field distortion effect gives an expected peak width of $\Delta t/t \approx 3 \times 10^{-3}$, in fair agreement with our observations. A reduction in the mesh spacing is expected to give a modest reduction in the width of the mass peaks, along with a major improvement in the attainable energy resolution.

An important issue that we have not yet investigated systematically is the transmission of the analyzer as a function of energy. Greater attention should be given to reducing stray electric and magnetic fields before attempting measurements with a monochromatic ion source of calibrated intensity. We expect the transmission to fall off rapidly for incident neutrals with energies less than 0.5 eV due to perturbations by the electron beam. In one respect this is actually an advantage, because the analyzer discriminates strongly against ions formed from residual gases in the detector chamber. Hence, the background resulting from the base pressure of the vacuum system is small relative to the signals from a directed beam as indicated by the size of the H_2O^+ peak in Figure 8.

REFERENCES

1. H. W. Kugel, G. M. Gammel, L. R. Grisham, R. Kaita, J. H. Kamperschroer, R. A. Langley, C. W. Magee, S. S. Medley, T. J. Murphy, A. L. Roquemore, and M. D. Williams, *Rev. Sci. Instrum.* 60, 37 (1989).
2. A. Faibus, W. Koenig, E. P. Kanter, and Z. Vager, *Nucl. Instrum. Meth.* B13, 673 (1986).
3. Y.-N. Chiu, B. Friedrich, W. Maring, G. Niedner, M. Noll, and J. P. Toennies, *J. Chem. Phys.* 88, 6814 (1988).
4. L. Shi, H. J. Frankena, and H. Mulder, *Rev. Sci. Instrum.* 60, 332 (1989).
5. B. Wilken, T. A. Fritz, and W. Studemann, *Nucl. Instrum. Meth.* 196, 161 (1982).
6. S. J. Bame, D. J. McComas, D. T. Young, and R. D. Belian, *Rev. Sci. Instrum.* 57, 1711 (1986).
7. H. Kuninaka, M. Ishii, and K. Kuriki, *J. Propulsion and Power*, 2, 408 (1986).
8. J. E. Polk, W. von Jaskowsky, A. J. Kelley, and R. G. Jahn, *J. Propulsion and Power*, 3, 33 (1987).
9. J. S. Sovey, *J. Spacecraft and Rockets*, 21, 483 (1984).
10. R. Dawbarn, R. L. McGuire, S. L. Steely, and J. G. Pipes, "Operating Characteristics of an Ablative Pulsed Plasma Engine," AEDC-TR-82-9, AFRPL-TR-82-17 (July 1982).
11. R. Bartiromo, G. Bracco, M. Brusati, G. Grosso, S. Mantovani, B. Tilia, and V. Zanza, *Rev. Sci. Instrum.* 58, 788 (1987).
12. A. L. Roquemore and S. S. Medley, *Rev. Sci. Instrum.* 57, 1797 (1986).
13. M. Neugebauer, D. R. Clay, B. E. Goldstein, and R. Goldstein, *Rev. Sci. Instrum.* 53, 277 (1982).
14. E. Leal-Quiros and M. A. Prelas, *Rev. Sci. Instrum.* 60, 350 (1989).
15. T. Matsuzawa, A. Takahashi, K. Masugata, M. Ito, M. Matsui, and K. Yatsui, *Rev. Sci. Instrum.* 56, 2279 (1985).
16. R. Weber, J. E. Balmer, and P. Ladrach, *Rev. Sci. Instrum.* 57, 1251 (1986).
17. M. J. Rhee, R. F. Schneider, and D. J. Weidman, *Rev. Sci. Instrum.* 58, 240 (1987).
18. C. J. Armentrout, G. Bramson, and R. Evanko, *Rev. Sci. Instrum.* 56, 2101 (1985).

19. R. K. Kirkwood, L. L. Higgins, J. Munch, and R. F. Wuerker, Rev. Sci. Instrum. 56, 1114 (1985).
20. J. A. Casey, S. F. Horne, J. H. Irby, R. S. Post, E. Sevillano, and J. H. Foote, Rev. Sci. Instrum. 59, 1664 (1988).
21. R. J. Colchin, A. L. Roquemore, and S. D. Scott, Rev. Sci. Instrum. 59, 1667 (1988).
22. W. W. Heidbrink, Rev. Sci. Instrum. 59, 1679 (1988).
23. H. Takeuchi, K. Tobita, Y. Kusama, M. Nemoto, T. Itoh, Y. Tsukahara, and JT-60 Team, Rev. Sci. Instrum. 59, 1652 (1988).
24. H. Verbeek, J. Phys. E: Sci. Instrum. 19, 964 (1986).
25. G. Hairapetian and R. L. Stenzel, Rev. Sci. Instrum. 58, 2099 (1987).
26. C. C. Petty, D. K. Smith, and D. L. Smatlak, Rev. Sci. Instrum. 59, 601 (1988).
27. W. C. Wiley and I. H. McLaren, Rev. Sci. Instrum. 26, 1150 (1955).
28. J. E. Pollard and R. B. Cohen, Rev. Sci. Instrum. 58, 32 (1987).
29. L. J. Richter and W. Ho, Rev. Sci. Instrum., 57, 1469 (1986).
30. B. A. Gurney, W. Ho, L. J. Richter, and J. S. Villarrubia, Rev. Sci. Instrum. 59, 22 (1988).
31. L. J. Richter, W. D. Mieber, L. J. Whitman, W. A. Noonan, and W. Ho, Rev. Sci. Instrum. 60, 12 (1989).
32. C. J. Armentrout, Rev. Sci. Instrum. 56, 1179 (1985).
33. F. P. Tully, N. H. Cheung, H. Haberland, and Y. T. Lee, J. Chem. Phys. 73, 4460 (1980).
34. D. M. Neumark, A. M. Wodtke, G. N. Robinson, C. C. Hayden, and Y. T. Lee, J. Chem. Phys. 82, 3045 (1985).
35. T. Bergmann, T. P. Martin, and H. Schaber, Rev. Sci. Instrum. 60, 347 (1989).

LABORATORY OPERATIONS

The Aerospace Corporation functions as an "architect-engineer" for national security projects, specializing in advanced military space systems. Providing research support, the corporation's Laboratory Operations conducts experimental and theoretical investigations that focus on the application of scientific and technical advances to such systems. Vital to the success of these investigations is the technical staff's wide-ranging expertise and its ability to stay current with new developments. This expertise is enhanced by a research program aimed at dealing with the many problems associated with rapidly evolving space systems. Contributing their capabilities to the research effort are these individual laboratories:

Aerophysics Laboratory: Launch vehicle and reentry fluid mechanics, heat transfer and flight dynamics; chemical and electric propulsion, propellant chemistry, chemical dynamics, environmental chemistry, trace detection; spacecraft structural mechanics, contamination, thermal and structural control; high temperature thermomechanics, gas kinetics and radiation; cw and pulsed chemical and excimer laser development, including chemical kinetics, spectroscopy, optical resonators, beam control, atmospheric propagation, laser effects and countermeasures.

Chemistry and Physics Laboratory: Atmospheric chemical reactions, atmospheric optics, light scattering, state-specific chemical reactions and radiative signatures of missile plumes, sensor out-of-field-of-view rejection, applied laser spectroscopy, laser chemistry, laser optoelectronics, solar cell physics, battery electrochemistry, space vacuum and radiation effects on materials, lubrication and surface phenomena, thermionic emission, photosensitive materials and detectors, atomic frequency standards, and environmental chemistry.

Electronics Research Laboratory: Microelectronics, solid-state device physics, compound semiconductors, radiation hardening; electro-optics, quantum electronics, solid-state lasers, optical propagation and communications; microwave semiconductor devices, microwave/millimeter wave measurements, diagnostics and radiometry, microwave/millimeter wave thermionic devices; atomic time and frequency standards; antennas, rf systems, electromagnetic propagation phenomena, space communication systems.

Materials Sciences Laboratory: Development of new materials: metals, alloys, ceramics, polymers and their composites, and new forms of carbon; nondestructive evaluation, component failure analysis and reliability; fracture mechanics and stress corrosion; analysis and evaluation of materials at cryogenic and elevated temperatures as well as in space and enemy-induced environments.

Space Sciences Laboratory: Magnetospheric, auroral and cosmic ray physics, wave-particle interactions, magnetospheric plasma waves; atmospheric and ionospheric physics, density and composition of the upper atmosphere, remote sensing using atmospheric radiation; solar physics, infrared astronomy, infrared signature analysis; effects of solar activity, magnetic storms and nuclear explosions on the earth's atmosphere, ionosphere and magnetosphere; effects of electromagnetic and particulate radiations on space systems; space instrumentation.